

www.acsami.org Research Article

Material-Dependent Evolution of Mechanical Folding Instabilities in Two-Dimensional Atomic Membranes

Jaehyung Yu, SunPhil Kim, Elif Ertekin, and Arend M. van der Zande*



Cite This: ACS Appl. Mater. Interfaces 2020, 12, 10801-10808



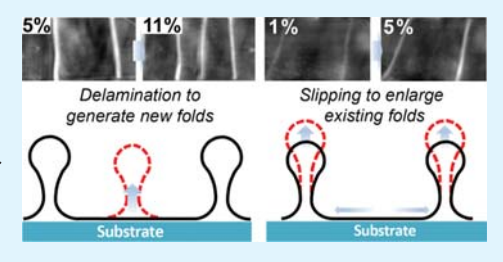
ACCESS

Metrics & More

Article Recommendations

Supporting Information

ABSTRACT: Inducing and controlling three-dimensional deformations in monolayer two-dimensional materials is important for applications from stretchable electronics to origami nanoelectromechanical systems. For these applications, it is critical to understand how the properties of different materials influence the morphologies of two-dimensional atomic membranes under mechanical loading. Here, we systematically investigate the evolution of mechanical folding instabilities in uniaxially compressed monolayer graphene and MoS_2 on a soft polydimethylsiloxane substrate. We examine the morphology of the compressed membranes using atomic force microscopy for compression



from 0 to 33%. We find the membranes display roughly evenly spaced folds and observe two distinct stress release mechanisms under increasing compression. At low compression, the membranes delaminate to generate new folds. At higher compression, the membranes slip over the surface to enlarge existing folds. We observe a material-dependent transition between these two behaviors at a critical fold spacing of 1000 ± 250 nm for graphene and 550 ± 20 nm for MoS_2 . We establish a simple shear-lag model which attributes the transition to a competition between static friction and adhesion and gives the maximum interfacial static friction on polydimethylsiloxane of 3.8 ± 0.8 MPa for graphene and 7.7 ± 2.5 MPa for MoS_2 . Furthermore, in graphene, we observe an additional transition from standing folds to fallen folds at 8.5 ± 2.3 nm fold height. These results provide a framework to control the nanoscale fold structure of monolayer atomic membranes, which is a critical step in deterministically designing stretchable or foldable nanosystems based on two-dimensional materials.

KEYWORDS: graphene, 2D materials, buckling, folding, adhesion, nanomechanics

1. INTRODUCTION

An important capability of soft materials and membranes is to relieve stress through the introduction of three-dimensional (3D) features like crumples, ripples, and folds. 1-3 These phenomena appear frequently in nature^{4,5} and are important to emerging nanotechnologies which couple 3D deformation to functionality like origami nanoelectromechanical systems^{6,7} and stretchable electronics.⁸⁻¹⁰ Monolayer two-dimensional (2D) materials like graphene and molybdenum disulfide are particularly relevant for understanding 3D deformation because they represent both the ultimate limit of mechanical atomic membranes 11-14 and molecular electronics. 15-18 Because of their exceptionally small bending moduli, it is easy to accidentally or intentionally induce 3D deformations in monolayer 2D materials, ^{12,19} which strongly affect the mechanics of the membrane. ^{13,20,21} Furthermore, the 3D morphologies impact the properties of monolayer 2D membranes, such as band gap^{22,23} and electronic conductivity. 24,25 Meanwhile, crumpling and folding in 2D material membranes (2D membranes) are currently being explored for applications as highly stretchable electronics, 26,27 3D architectures for catalysis, 28 and mechanically reconfigurable origami and kirigami systems.¹⁹ In all these applications, an important challenge is to understand, predict, and control the

constituent relations between induced stresses, material and substrate properties, and the resulting 3D morphologies.

Introducing tensile or compressive strains on 2D membranes laminated onto soft, stretchable substrates is a useful strategy for inducing deformations because the strain is reversible, and the structures are easily integrated into devices for applications. ^{27,29} Crumples in compressed 2D membranes have been shown to strongly affect many multifunctional properties of 2D materials including optical absorption, ^{30–32} hydrophobicity, ²⁷ and chemical reactivity. ³³ While there have been a number of experimental ^{34–41} and theoretical studies ^{42–45} of the structure and mechanics of crumpling, there is still a need to systematically understand the evolution of the 3D morphology of compressed 2D membranes. Different studies display widely varying behavior including rippling, folding, buckling delamination, and crumpling and yet are difficult to compare because they are performed on structures under high compression (>100%), ^{30,31,39} different materi-

Received: November 17, 2019 Accepted: February 10, 2020 Published: February 10, 2020



als^{32,35,46} with fixed and different strains^{34,36,40,42-44} or different thickness.⁴⁷ Comparing these studies is challenging, as crumpling instabilities are intrinsically statistical processes, with no global solutions. Recent papers on the crumpling of thin films^{5,48,49} or multilayer 2D material membranes with several nanometer thickness show buckle delamination and rippling in which the morphology is dominated by the bending modulus. 39,40,50-54 In contrast, 2D monolayer membranes have very small bending modulus;⁵⁵ so the morphology is dominated by the interface.^{24,37,55,56} While the compression mechanics of thin film and multilayer structures are relatively well understood, models are needed that relate the formation and evolution of mechanical instabilities in the 2D monolayer membrane limit. Understanding and relating the behavior of different materials over a range of strains gives insight into the behavior at all scales and has the utility in guiding the design of desired morphologies for applications such as stretchable electronics from crumpled 2D heterostructures or spatially tailoring material properties under deformation.

Here, we quantify and compare the material-dependent evolution of 3D morphologies occurring in monolayer graphene and MoS₂ under systematically varied uniaxial compressive strain on a polydimethylsiloxane (PDMS) substrate and establish a model which describes the behavior in both materials based solely on mechanical properties. Both 2D membranes displayed roughly evenly spaced folds under uniaxial compression.

We find that at small compressions, 2D membranes relieve stress via delamination and the introduction of roughly evenly spaced folds. At higher compression above 10%, the membranes relieve stress via interfacial slip and increasing the size of existing folds. The transition between these two stress relief mechanisms is material-dependent, occurring when the folds reach a critical period of 1000 ± 250 nm for graphene and 550 \pm 20 nm for MoS₂. We established a continuum shear-lag model wherein the compression on the 2D membrane is induced by the surface traction at the interface between the membrane and the substrate. In this model, delamination occurs when the compressive energy in the membrane exceeds the adhesion energy and slip occurs when the surface traction exceeds the maximum static friction. The competition between these two phenomena explains the material-dependent transition in fold spacing and enables extraction of the interfacial friction between the 2D membrane and substrate from the experimental results. We find the maximum interfacial static friction on PDMS is 3.8 ± 0.8 MPa for graphene and 7.7 ± 2.5 MPa for MoS₂. Moreover, graphene displayed an additional mechanism not observed in MoS2 in which standing folds transitioned to fallen folds around 8.5 \pm 2.3 nm fold height, after which the fallen folds then increased in width under increasing compression. These results demonstrate that the transitions between fold delamination and slip, and from standing to fallen folds, depend on the local features of fold spacing and height rather than global parameters like substrate strain.

2. EXPERIMENTAL SECTION

Figure 1 shows the structures used to measure the 3D morphology of 2D membranes under uniaxial compression. As shown in Figure 1a, the devices were fabricated by transferring monolayer graphene or monolayer MoS_2 onto a prestrained PDMS substrate and then released to form folds. The full fabrication details are found in Supporting Information Section S1. Briefly, for the 2D materials, we

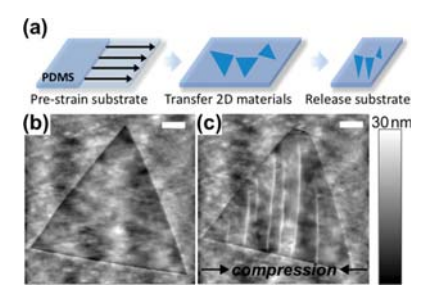


Figure 1. Inducing compression in 2D materials. (a) Schematic of the fabrication process for inducing compression of 2D monolayers on a PDMS substrate. (b,c) AFM topography images of a CVD grown monolayer MoS_2 triangle on PDMS (b) before and (c) after 8% compression along the horizontal direction. Before compression, the monolayer follows the surface roughness of the substrate. After compression, roughly evenly spaced folds are observed along the direction of compression. Scale bar = 2 μ m.

used chemical vapor deposition (CVD) monolayer MoS2 and mechanically exfoliated monolayer graphene, both on a 285 nm silicon oxide on a silicon substrate. The monolayer structure is confirmed with Raman and photoluminescence spectroscopy, as shown in Supporting Information Figure S1. $^{57-59}$ CVD-grown graphene was not used because the roughness of the copper growth substrate frequently leads to preexisting folds when transferred. We then transferred the 2D monolayers onto uniaxially prestrained PDMS substrates using a dry transfer process. 60 The PDMS substrates were mounted on a custom holder, as shown in Supporting Information Figure S2, which allowed us to fix and vary the uniaxial strain on the 2D membrane in a range from 0 to 50%. The prestrain in the substrates were subsequently released by fixed increments, leading to a controlled and increasing uniaxial compressive strain on the 2D monolayers. As shown in Supporting Information Figure S3, we ensure accurate estimate of the overall compressive strain of the 2D monolayers⁴¹ by measuring the change in separation of well-defined landmark features of 2D monolayers with an optical microscope rather than computing strain from the substrate deformation.

We measured the nanoscale morphology of the membranes with atomic force microscopy (AFM). Figure 1b,c shows the morphology of a single crystal triangle of CVD-grown monolayer MoS_2 after transfer onto a prestrained substrate and after 8% compression. Before compression, the membranes are flat, with a root mean square surface roughness of 0.9 nm, similar to the surface roughness of the underlying substrate of 1.0 nm. After compression, the MoS_2 displays roughly evenly spaced folding along the direction of compression with fold heights in the range of S-15 nm and spacings that range from 0.9 to $1.1~\mu m$. Between the folds, the roughness of the MoS_2 surface increases slightly to 1.8 nm while the substrate remains the same at 1.0 nm

3. RESULTS AND DISCUSSION

Figures 2 and 3 directly compare the evolution in morphology of single regions of monolayer MoS₂ with monolayer graphene respectively under increasing substrate compression. From the measurements, we observed two distinctive stress release mechanisms leading to the change in the membrane morphology: (i) slip to enlarge existing folds and (ii) delamination to generate new folds. Figure 2a—d shows topographic AFM images of a single region of monolayer MoS₂ under increasing uniaxial compression from 5 to 19%, while Figure 2e shows the cross-section height profile of the same region at different compression, indicated by the colored lines in each AFM image. Initially, as the compression increases, the MoS₂ membrane is delaminated from the substrate and generates new folds approximately halfway between the

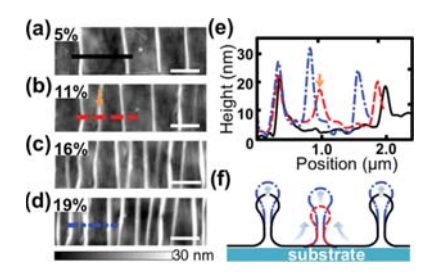


Figure 2. Evolution of MoS2 folds under increasing compression. (a–d) Sequence of AFM topography images showing the change in the 3D morphology of a single region of monolayer MoS2 under increasing compression of 5, 11, 16, and 19%, respectively. Scale bar = 1 μ m. (e) Corresponding height profile of the same position at different compressions indicated by the black, red, and blue lines shown respectively in (a,b,d). Between 5 and 11% a new fold is nucleated, marked by the orange arrow in both (b,e). (f) Schematic of the change in fold morphologies corresponding to the region shown in (e). Red corresponds to new fold generation, and blue corresponds to slip and growth of existing folds.

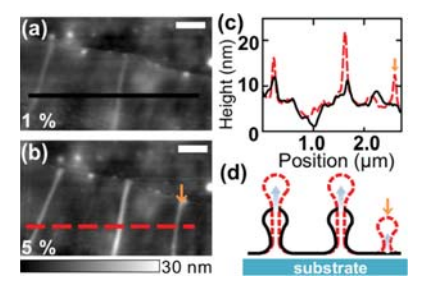


Figure 3. Evolution of graphene folds under increasing compression. (a,b) Sequence of AFM topography images showing the change in the 3D morphology of a single region of monolayer exfoliated graphene under increasing compression of 1 and 5%, respectively. Orange arrow in (b) shows newly generated fold. (c) Corresponding height profile of the same position at different compression indicated by black and red lines shown respectively in (a,b). (d) Schematic of the change in fold morphologies corresponding to the region shown in (c). Both enlargement of existing folds and new fold generation occur.

existing folds, for example, at the orange arrow in Figure 2b. Indicated in the red line in Figure 2e, the height of preexisting folds does not change significantly, while the new folds quickly grow to the height of the preexisting folds. For higher compressions, for example, when going from 11% (red line) to 19% (blue line), rather than delamination, the average height of the folds increased by slip. Figure 2f shows schematically the processes for delamination versus slip. Supporting Information Figure S4 contains additional AFMs of MoS2 at different compression values, which show the same qualitative behavior, and Supporting Information Figure S5 shows the fold evolution when restretching the substrate. As a result of the ultra-low bending modulus in 2D monolayers, these folds have a hairpin geometry consistent with previous simulations⁵⁶ and experiments, ^{24,37,38,61} rather than a buckle-delamination geometry commonly observed in multilayer structures 50,52,62 or thin films. 48,63 As seen in Supporting Information Figures S4-S6, the AFM profiles of the folds at low compression have a single narrow peak with a measured width of <5 nm for graphene and 10-50 nm MoS₂ after deconvolving the shape of the tip. These narrow widths support the hairpin geometry.

Figure 3 shows similar analysis performed on exfoliated monolayer graphene under increasing compression. Figure

3a,b shows the same region of graphene folds for compressive strains of 1 and 5%, while Figure 3c shows the corresponding cross-section height profiles. At small compression, the graphene also displays delamination, shown by the orange arrow in Figure 3b, in addition to some degree of slip to the existing fold growth. Figure 3d shows the schematic of the slip while partially delaminating membranes. Supporting Information Figure S6 contains additional images of graphene under varying compression. Unlike MoS₂, the transition to slip to enlarge existing folds occurs at much lower compression and higher fold spacing.

In Figures 2 and 3, we observe both stress release mechanisms, delamination and slip, in both materials, and they appear at different compression levels. However, because mechanical folding instabilities from stress release mechanisms are a stochastic process, there is significant variation in the spacing between folds and global behavior cannot be inferred from a single region. To quantitatively determine the mechanics of the monolayer membranes, it is necessary to perform a statistical analysis.

In Figure 4, we compare the average behavior of multiple regions under increasing compression. The key parameters

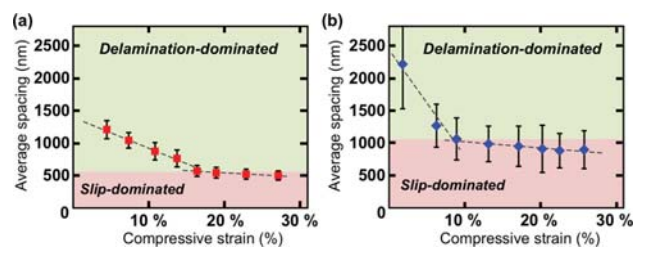


Figure 4. Induced average spacing between folds in compressed 2D membranes. (a) Average fold spacing in monolayer MoS_2 measured in seven different sample locations. (b) Average fold spacing in monolayer graphene vs compression measured in five different exfoliated samples. The lines indicate the rate of change of the spacing between folds vs compression. For low compression, the spacing between folds in MoS_2 and graphene respectively change at a rate of 47 and 162 nm/%. For higher compression, the rates become 6 and 10 nm/%, respectively. In both materials, there is a transition in behavior at 550 ± 20 and 1000 ± 250 nm, respectively. The transition point corresponds with a change in the stress release mechanism from delamination-dominated to generate new folds toward slip-dominated to enlarge existing folds.

extracted from the fold topography are the average height, average width, and average period of folds. However, due to AFM tip interactions ^{64,65} and scan conditions (see Supporting Information Figure S7), it is difficult to accurately measure the height and width of soft folds, making the average period a more reliable measure for comparison. Figures 4a,b, respectively, plot the average fold period versus compression for MoS₂ and graphene. The MoS₂ data were averaged over seven different monolayers on the same substrate, while the graphene data were averaged over five different exfoliated monolayers. In MoS₂, for small compression of <16%, the average period reduces at a rate of 47 nm/%. This rate is much larger than the rate expected purely from compression of 12 nm/%. The rate of change in the period undergoes a sudden kink at 16% compression to the rate of 6 nm/%. As shown in Figure 4b, similar behavior is also observed in the exfoliated graphene compression. For small compression, the graphene period reduces at a rate of 162 nm/%. Around 8%

compression, the rate changes to 10 nm/%. The rapid reduction of fold spacing at small strains corresponds to delamination to generate new folds, leading to a smaller period. At higher compression, the strain is instead accommodated via membrane slip leading to the increase in the size of existing folds with a rate of change similar to that expected from pure compression. The transition occurs in MoS₂ and graphene at compressions of 16 and 8% respectively, which is a reflection of their different mechanical properties. As a final observation, the spacing in the folds are more irregular in the graphene than the MoS₂ leading to the larger error bars observed in Figure 4b. We hypothesize that the increased irregularity is a result of the larger period overall in the graphene folds. The precise point of fold generation will be affected by nanoscale inhomogeneities like particles at the interface, concentration of forces at edges, shape of the compressed 2D membrane, 41 and surface roughness.44 Thus, a larger period between folds allows for increased deviation in where the new folds are generated.

Figure 5 describes a continuum shear-lag model we developed 66 to explain the observed evolution in morphology.

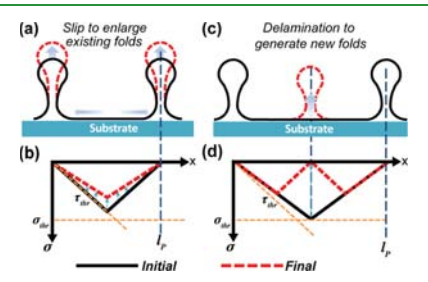


Figure 5. Model of stress release mechanisms in compressed 2D monolayers. (a) Schematic of the change in morphology for a membrane that has reached the maximum static friction $\tau_{\rm thr}$ to undergo slip and enlargement of the existing folds. (b) In-plane stress vs position profile corresponding with the change in compression from (a) assuming a constant surface traction at the membrane and substrate interface. The final (red) stress profile has higher max stress and slope than the initial (black) profile. (c,d) Similar schematic and stress profile where the max stress at the center has exceeded threshold $\sigma_{\rm thr}$ which corresponding to the adhesion energy resulting in the membrane locally delaminating to generate a new fold.

We adapt existing models on interfacial sliding 34 and buckling of tensioned or compressed 2D materials on a soft substrate 35,36,44 to describe how the existing stress distribution from a current configuration (fold height, spacing, and strain) will evolve when an additional compressive strain is introduced. We assume that uniaxial substrate compression leads to the application of a uniform surface traction τ at the 2D material surface oriented along the direction of the compression. This surface traction depends on the interaction of the 2D membrane with the substrate including surface roughness and adhesion, intercalated water or surface contamination, as well as the substrate mechanical moduli leading to strain transfer. Together, these contributions lead to an effective shear stress applied to the 2D material by the substrate wherein only the mechanics of the membrane need to be considered. The in-plane stress distribution in the 2D material is related by the one-dimensional equilibrium equation.

$$\tau = \frac{\mathrm{d}\sigma}{\mathrm{d}x} \tag{1}$$

For uniform τ , eq 1 indicates that the resulting in-plane stress $\sigma(x)$ in the 2D material is linear along the direction of compression and uniform through the interface between the 2D membrane and the substrate.⁴⁴

When a new fold forms, the built-up compressive stress is locally relieved. Because the bending stiffness of monolayer graphene is orders of magnitude lower than the Young's modulus¹⁹ and adhesion energy, ^{35,69-71} the predicted average compressive strain on the nanometer scale curvatures of the hairpin folds corresponds to <0.03-0.07% for the average height of the measured folds, which is much lower than the induced compressive strains on the laminated regions of the monolayers. As a result, we can reasonably assume the residual in-plane stress within the delaminated folds to be effectively zero, 24,56 compared with the laminated regions between the folds. In equilibrium, the size of the fold between slip events is fixed because the surface traction is much larger than the selfadhesion of the 2D material in the fold, preventing the pulling of the new material into the fold. Taken together, the stress within the 2D membrane is zero at the folds and increases in magnitude linearly with slope τ away from each fold, with a peak in stress $|\sigma_{max}|$ halfway between neighboring folds. From the geometry, the relationship between the maximum stress magnitude, interfacial stress due to compression, and fold spacing $l_{\rm p}$ is

$$|\sigma_{\text{max}}| = \tau(l_{\text{p}}/2) \tag{2}$$

Figure 5a,c shows schematically a 2D membrane with periodic folds undergoing slip or delamination stress relief mechanisms, while Figure 5b,d shows the corresponding stress distribution $\sigma(x)$ within the membrane versus the position for each mechanism according to our model. The black and red dashed lines represent the morphology and stress distribution immediately before and after slip or delamination, respectively.

According to the model, as substrate compression increases, the folds move closer to each other, the stress slope increases, and the maximum compressive stress magnitude increases. The slope and max stress will both increase under increasing compression until one of the two thresholds are reached. Figure 5a,b shows slipping to grow existing folds: if the slope of the stress profile exceeds a threshold $|\tau| \leq \tau_{\text{thr}}$ corresponding to the maximum static friction of the 2D material on the substrate, then the membrane will slip at the site of an existing fold, leading to an increase in the size of the fold and a drop in τ . The adhered portion of the membrane will locally slip until reaching a new equilibrium residual stress indicated by the red dashed line in Figure 5b. The relative slope and shape of the residual stress after slip will be determined by the dynamic friction of the interface compared with the static friction. ⁶⁶

Delamination to form new folds is shown in Figure 5c,d: if the maximum stress halfway between the folds exceeds a stress threshold $|\sigma_{\rm max}| \leq \sigma_{\rm thr}$ corresponding with in-plane stress exceeding the delamination energy of the substrate, then a spontaneous delamination will occur, leading to a new fold, a reduction of $|\sigma_{\rm max}|$, and a new stress profile shown as the red dashed line in Figure 5d. At the point and instant of delamination, the membrane goes from a flat, adhered state to a nanoscale buckle-delamination, 56 which will locally have a stress near zero. This difference in stress will cause the membrane to locally slip, providing new material to the delaminated region. Because of the low bending modulus and high self-adhesion of the 2D material, the delaminated region will collapse to form the fold. 24,36 Shown as the red dashed line

in Figure 5d, after new fold generation is complete, the stress profile splits into two new profiles with half the period. The energetics and dynamics of this sequence is complex. Importantly though, we note that membrane delamination is an instability similar to Euler buckling, ^{48,63} wherein the onset is predicted from the point at which a solution becomes unstable, rather than from energy conservation between the initial and final shape of the structure. ⁶⁶ As a result, it is unnecessary to account for the energetics or dynamics of the folding process or self-adhesion of the membrane in the fold to predict the onset of delamination.

The delamination will occur at the point of highest stress. From energy conservation, the threshold compressive stress $\sigma_{\rm thr}$ for the onset of delamination is related to the adhesion energy per unit area Γ between the substrate and the 2D membrane 63

$$\frac{1}{2E_{\rm 2D}}\sigma_{\rm thr}^2 = \Gamma \tag{3}$$

where $E_{\rm 2D}$ is the 2D Young's modulus of the membrane.

Whether slip or delamination will occur is determined by whether the slope of the stress profile reaches $\tau_{\rm thr}$ or the max stress reaches $\sigma_{\rm thr}$ first. As indicated in Figure 5c,d, for longer fold periods and lower compression, delamination will occur first, while for shorter fold periods, slip will occur first. The fold period $l_{\rm transition}$ corresponding to the transition from new fold generation to growth of existing folds arises from combining eqs 1–3 at the interfacial and delamination thresholds

$$\tau_{\rm thr} \frac{l_{\rm transition}}{2} = \sigma_{\rm thr} = \sqrt{2E_{\rm 2D}\Gamma} \tag{4}$$

Equation 4 and the experimental measurements of $l_{\rm transition}$ from Figure 4 (1000 ± 250 nm in graphene, 550 ± 20 nm in MoS₂) determine the value of $\tau_{\rm thr}$ for each 2D material. Using the 2D modulus 72,73 and adhesion energy, $^{35,69-71}$ the maximum interfacial static friction before slip is determined to be $\tau_{\rm thr}=3.0-4.6$ MPa in graphene and $\tau_{\rm thr}=5.2-10.2$ MPa in MoS₂. The corresponding compressive stress and strain on the adhered region before delamination will be $\sigma_{\rm thr}=1.4-2.3$ N/m and $\varepsilon_{\rm thr}=0.4-0.7\%$ for graphene and $\sigma_{\rm thr}=1.4-2.8$ N/m and $\varepsilon_{\rm thr}=0.8-1.6\%$ for MoS₂. The numerical values are summarized in Supporting Information Table S1. These values are similar to the onset of slip of 1.2–1.5% in systems under tensile strain. $^{34-36,41}$

This model is formulated so that the only critical parameters are σ_{thr} and τ_{thr} , and the evolution of the folding morphology depends on the initial conditions and compression history. As with many crumpling phenomena, the transition depends on the initial fold structure present and the compression history and can occur at different values of these parameters; thus there is no global threshold value for substrate strain, fold height, or fold spacing for the transition from new fold generation to growth of existing folds. Moreover, surface traction is a measure of the effective force acting on the membrane, and the model does not consider the origin of the surface traction which is substrate material-dependent. We expect this model to be generalizable to the compression of isotropic, thin, flexible membranes under uniaxial compression on a soft substrate, which possesses low friction interfaces to allow slip the membrane on the substrate surface.

As we continue to increase the compression of the substrate, we observe an additional transition in fold morphologies in the

monolayer graphene. Figure 6a-c shows the enlarged images of a single graphene fold under increasing compression from 5

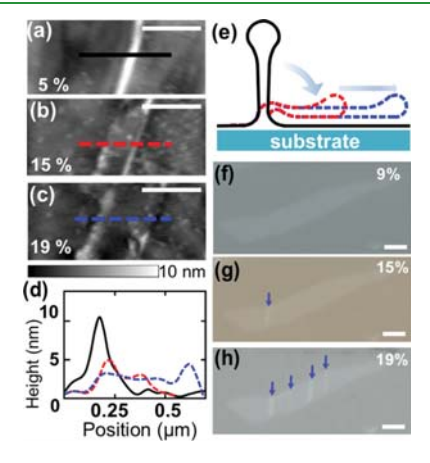


Figure 6. Collapse of folds at higher compression. (a–c) Sequence of topography images zoomed in onto a single graphene fold under increasing compression of 5, 15, and 19% respectively. Scale bar = 0.5 μ m. (d) Corresponding height profile of the same fold at different compression indicated by the black red and blue lines shown respectively in (a–c). (e) Schematic of the transition from a standing to fallen fold corresponding with the region shown in (d). (f–h) Optical microscope images of monolayer graphene under increasing compression of 9, 15, and 19%, respectively. Arrow marks fallen folds appeared by different contrast. Scale bar = 2 μ m.

to 19%, while Figure 6d shows the corresponding crosssectional height profiles. At small compression, the fold has a narrow profile of a standing fold. At higher compression, the height drops from 10 to <5 nm, and a second short peak appears adjacent to the initial peak. We associate this new profile with a fallen fold where the additional layers lay over the underlying monolayer. Both standing and fallen folds are often observed in graphene conformally grown on a rough copper foil that is subsequently transferred onto flatter substrates²⁴ or by differential shrinkage during cooling in graphene grown on silicon carbide. These previous studies found that there is a critical height at which fallen folds become more energetically favorable 24,37,38 than the standing fold. In those cases, the folds are induced by an extra slack in the graphene, whereas here we controllably induce falling of the folds. Indeed, under varying compression, we observe a transition of the standing fold (Figure 6a) to a fallen fold (Figure 6b), which subsequently keeps broadening in width upon further compression (Figure 6c). The whole process is shown schematically in Figure 6d.

Figure 6f—h shows a sequence of optical images of the evolution of several folds on a single piece of graphene under increasing compression. Because the standing folds are very narrow, they are difficult to see optically. However, the fallen folds are easy to see as they lead to a change in contrast from the three layers stacked on top of each other. These images show that, rather than all folds falling simultaneously at a particular compression, the falling transition is related to the height of the individual folds. From eleven different folds measured through a range of strains, the average height of the folds before falling was 8.5 \pm 2.3 nm. In general, in buckledelamination features, the falling transition will depend on the aspect ratio of height to width. 24,38 However, in the case of the

hairpin geometry fold, the height of the fold is the only critical parameter because the width of the fold is a constant.

We note, as discussed earlier and shown in Supporting Information Figure S7, the measurement of the fold height and width of the folds with AFM is less accurate than the measurement in spacing due to the tip interactions and scan response, with nanoscale feature width being especially difficult to measure accurately. As a result, caution should be used in overinterpreting the accuracy of the height and we only present the critical height as opposed to an aspect ratio. Furthermore, we note that AFM measures the static states between transitions induced during the straining, not the dynamics of the folding process. Following the established dynamics of many mechanical instabilities, we hypothesize that the falling of the fold is instigated at a point of lower stability, such as at a bump on the substrate, a point of intersecting folds, or at the edge of the membrane, then zips along the fold until it reaches some point of higher stability.

We follow previous models to calculate the relative energy of standing versus fallen folds^{24,38} (details in Supporting Information Section S3). We note that the analysis of standing to fallen fold transition is different from the mechanical instabilities such as the onset of delamination or slip presented earlier. The relative total energies between initial and final states in the standing to fallen fold transition, rather than the point at which a particular state becomes unstable, govern the transition. The analysis shows that the standing fold is always dynamically stable but is energetically unfavorable compared with the fallen fold above the critical height. Above the critical height, small perturbations, inhomogeneous strain, or thermal fluctuations may induce the fold to fall into the more energetically favorable morphology. From the above calculations, the threshold height in graphene is predicted to be 6 nm, which occurs ~5% compression in this study. From the same analysis, the critical height of MoS₂ is \sim 19 nm, which will only occur at compressions above those induced in this study. We note that these models do not include the influence of important factors like substrate roughness, folds not being perfectly perpendicular to the direction of strain, induced shears, or pre-existing corrugations, all of which could effectively stiffen the membrane and lead to the significant variation we observe in the critical height.

4. CONCLUSIONS

To summarize, we observe and explain two different stress release mechanisms occurring in 2D materials graphene and MoS₂ under compression: (i) slip to enlarge existing folds and (ii) delamination to generate new folds. Furthermore, in graphene, we observed the transition of fold morphologies from standing to fallen folds with increasing substrate compression. We show that these transitions in behavior are material-dependent and sensitive to interfacial properties such as adhesion and maximum static friction with the substrate. Moreover, the transitions between fold delamination and slip and from standing to fallen folds depend on the local features of fold spacing and height rather than global parameters like substrate strain. This understanding of the origins and evolution of 3D deformation with systematically varied levels of compression gives the potential to control the nanoscale fold structure of 2D atomic membranes, which is a critical step in deterministically engineering stretchable, foldable 3D systems based on 2D materials. For example, these results show that crumpled 2D devices, which often depend on high

compression >100%, likely contain multilayer folds. Next steps include understanding the impact of rate dependence and substrate properties on adhesion and the resulting morphology, extending the model to incorporate biaxial compression, and studying the mechanics of 2D membranes from heterostructures which exhibit slip and superlubricity at the interfaces between layers as well as at the substrate.

ASSOCIATED CONTENT

Supporting Information

The Supporting Information is available free of charge at https://pubs.acs.org/doi/10.1021/acsami.9b20909.

Details on sample preparation, measuring fold morphology, and predicting threshold height of fold collapse (PDF)

AUTHOR INFORMATION

Corresponding Author

Arend M. van der Zande — Department of Mechanical Science and Engineering and Materials Research Laboratory, University of Illinois at Urbana-Champaign, Urbana, Illinois 61801, United States; orcid.org/0000-0001-5104-9646; Email: arendv@illinois.edu

Authors

Jaehyung Yu — Department of Mechanical Science and Engineering, University of Illinois at Urbana-Champaign, Urbana, Illinois 61801, United States; ⊙ orcid.org/0000-0002-9925-2309

SunPhil Kim — Department of Mechanical Science and Engineering, University of Illinois at Urbana-Champaign, Urbana, Illinois 61801, United States; ⊙ orcid.org/0000-0002-5627-1139

Elif Ertekin — Department of Mechanical Science and Engineering and Materials Research Laboratory, University of Illinois at Urbana-Champaign, Urbana, Illinois 61801, United States; o orcid.org/0000-0002-7816-1803

Complete contact information is available at: https://pubs.acs.org/10.1021/acsami.9b20909

Author Contributions

A.M.v.d.Z. and J.Y. conceived the idea and designed the experiments. J.Y. and S.K conducted material growth. J.Y conducted device fabrication, measurements, and analyzed the data. A.M.v.d.Z, J.Y, and E.E developed the model. All authors contributed to writing the manuscript.

Notes

The authors declare no competing financial interest.

ACKNOWLEDGMENTS

This research was primarily supported by the National Science Foundation MRSEC program under NSF award number DMR-1720633. S.K. was supported by the National Science Foundation CAREER program, under NSF award number CMMI-1846732. This work was carried out in the Fredrick-Seitz Material Research Laboratory Central Facilities and the Micro and Nano Technology Laboratory. We thank Jangyup Son, Mohammad Abir Hossain, Dongyun Kang, Yunjo Jeong, Narayan Aluru, Nadya Mason, Sungwoo Nam, and Pinshane Huang for helpful discussions.

■ REFERENCES

- (1) Kim, P.; Abkarian, M.; Stone, H. A. Hierarchical Folding of Elastic Membranes under Biaxial Compressive Stress. *Nat. Mater.* **2011**, *10*, 952–957.
- (2) Pocivavsek, L.; Dellsy, R.; Kern, A.; Johnson, S.; Lin, B.; Lee, K. Y. C.; Cerda, E. Stress and Fold Localization in Thin Elastic Membranes. *Science* **2008**, 320, 912–916.
- (3) Cerda, E.; Mahadevan, L. Geometry and Physics of Wrinkling. *Phys. Rev. Lett.* **2003**, *90*, 074302.
- (4) Li, B.; Cao, Y.-P.; Feng, X.-Q.; Gao, H. Mechanics of Morphological Instabilities and Surface Wrinkling in Soft Materials: A Review. *Soft Matter* **2012**, *8*, 5728.
- (5) Wang, Q.; Zhao, X. A Three-Dimensional Phase Diagram of Growth-Induced Surface Instabilities. Sci. Rep. 2015, 5, 8887.
- (6) Shenoy, V. B.; Gracias, D. H. Self-Folding Thin-Film Materials: From Nanopolyhedra to Graphene Origami. *MRS Bull.* **2012**, *37*, 847–854.
- (7) Huntington, M. D.; Engel, C. J.; Odom, T. W. Controlling the Orientation of Nanowrinkles and Nanofolds by Patterning Strain in a Thin Skin Layer on a Polymer Substrate. *Angew. Chem., Int. Ed.* **2014**, 53, 8117–8121.
- (8) Rogers, J. A.; Someya, T.; Huang, Y. Materials and Mechanics for Stretchable Electronics. *Science* **2010**, *327*, 1603–1607.
- (9) Kim, D. H.; Rogers, J. A. Stretchable Electronics: Materials Strategies and Devices. *Adv. Mater.* **2008**, *20*, 4887–4892.
- (10) Lipomi, D. J.; Bao, Z. Stretchable and Ultraflexible Organic Electronics. MRS Bull. 2017, 42, 93–97.
- (11) Akinwande, D.; Brennan, C. J.; Bunch, J. S.; Egberts, P.; Felts, J. R.; Gao, H.; Huang, R.; Kim, J.-S.; Li, T.; Li, Y.; Liechti, K. M.; Lu, N.; Park, H. S.; Reed, E. J.; Wang, P.; Yakobson, B. I.; Zhang, T.; Zhang, Y.-W.; Zhou, Y.; Zhu, Y. A Review on Mechanics and Mechanical Properties of 2D Materials—Graphene and Beyond. *Extrem. Mech. Lett.* **2017**, *13*, 42–77.
- (12) Bao, W.; Miao, F.; Chen, Z.; Zhang, H.; Jang, W.; Dames, C.; Lau, C. N. Controlled Ripple Texturing of Suspended Graphene and Ultrathin Graphite Membranes. *Nat. Nanotechnol.* **2009**, *4*, 562–566.
- (13) Bunch, J. S.; Verbridge, S. S.; Alden, J. S.; van Der Zande, A. M.; Parpia, J. M.; Craighead, H. G.; McEuen, P. L. Impermeable Atomic Membranes from Graphene Sheets. *Nano Lett.* **2008**, *8*, 2458–2462
- (14) Bunch, J. S.; van der Zande, A. M.; Verbridge, S. S.; Frank, I. W.; Tanenbaum, D. M.; Parpia, J. M.; Craighead, H. G.; McEuen, P. L. Electromechanical Resonators from Graphene Sheets. *Science* **2007**, *315*, 490–493.
- (15) Lee, C.-H.; Lee, G.-H.; van der Zande, A. M.; Chen, W.; Li, Y.; Han, M.; Cui, X.; Arefe, G.; Nuckolls, C.; Heinz, T. F.; Guo, J.; Hone, J.; Kim, P. Atomically Thin p—n Junctions with van Der Waals Heterointerfaces. *Nat. Nanotechnol.* **2014**, *9*, 676–681.
- (16) Eda, G.; Fanchini, G.; Chhowalla, M. Large-Area Ultrathin Films of Reduced Graphene Oxide as a Transparent and Flexible Electronic Material. *Nat. Nanotechnol.* **2008**, *3*, 270–274.
- (17) Kim, K. S.; Zhao, Y.; Jang, H.; Lee, S. Y.; Kim, J. M.; Kim, K. S.; Ahn, J.-H.; Kim, P.; Choi, J.-Y.; Hong, B. H. Large-Scale Pattern Growth of Graphene Films for Stretchable Transparent Electrodes. *Nature* **2009**, 457, 706–710.
- (18) Geim, A. K.; Grigorieva, I. V. Van Der Waals Heterostructures. *Nature* **2013**, 499, 419–425.
- (19) Blees, M. K.; Barnard, A. W.; Rose, P. A.; Roberts, S. P.; McGill, K. L.; Huang, P. Y.; Ruyack, A. R.; Kevek, J. W.; Kobrin, B.; Muller, D. A.; McEuen, P. L. Graphene Kirigami. *Nature* **2015**, *524*, 204–207.
- (20) Booth, T. J.; Blake, P.; Nair, R. R.; Jiang, D.; Hill, E. W.; Bangert, U.; Bleloch, A.; Gass, M.; Novoselov, K. S.; Katsnelson, M. I.; Geim, A. K. Macroscopic Graphene Membranes and Their Extraordinary Stiffness. *Nano Lett.* **2008**, *8*, 2442–2446.
- (21) Garcia-Sanchez, D.; van der Zande, A. M.; Paulo, A. S.; Lassagne, B.; Mceuen, P. L.; Bachtold, A. Imaging Mechanical Vibrations in Suspended Graphene Sheets. *Nano Lett.* **2008**, *8*, 1399–1403.

- (22) Feng, J.; Qian, X.; Huang, C.-W.; Li, J. Strain-Engineered Artificial Atom as a Broad-Spectrum Solar Energy Funnel. *Nat. Photonics* **2012**, *6*, 866–872.
- (23) Li, H.; Contryman, A. W.; Qian, X.; Ardakani, S. M.; Gong, Y.; Wang, X.; Weisse, J. M.; Lee, C. H.; Zhao, J.; Ajayan, P. M.; Li, J.; Manoharan, H. C.; Zheng, X. Optoelectronic Crystal of Artificial Atoms in Strain-Textured Molybdenum Disulphide. *Nat. Commun.* **2015**, *6*, 7381.
- (24) Zhu, W.; Low, T.; Perebeinos, V.; Bol, A. A.; Zhu, Y.; Yan, H.; Tersoff, J.; Avouris, P. Structure and Electronic Transport in Graphene Wrinkles. *Nano Lett.* **2012**, *12*, 3431–3436.
- (25) Tapasztó, L.; Dumitrică, T.; Kim, S. J.; Nemes-Incze, P.; Hwang, C.; Biró, L. P. Breakdown of Continuum Mechanics for Nanometre-Wavelength Rippling of Graphene. *Nat. Phys.* **2012**, *8*, 739–742.
- (26) Wang, Y.; Yang, R.; Shi, Z.; Zhang, L.; Shi, D.; Wang, E.; Zhang, G. Super-Elastic Graphene Ripples for Flexible Strain Sensors. *ACS Nano* **2011**, *5*, 3645–3650.
- (27) Zang, J.; Ryu, S.; Pugno, N.; Wang, Q.; Tu, Q.; Buehler, M. J.; Zhao, X. Multifunctionality and Control of the Crumpling and Unfolding of Large-Area Graphene. *Nat. Mater.* **2013**, *12*, 321–325.
- (28) Chen, P.-Y.; Liu, M.; Wang, Z.; Hurt, R. H.; Wong, I. Y. From Flatland to Spaceland: Higher Dimensional Patterning with Two-Dimensional Materials. *Adv. Mater.* **2017**, *29*, 1605096.
- (29) Kang, P.; Wang, M. C.; Knapp, P. M.; Nam, S. Crumpled Graphene Photodetector with Enhanced, Strain-Tunable, and Wavelength-Selective Photoresponsivity. *Adv. Mater.* **2016**, *28*, 4639–4645.
- (30) Leem, J.; Wang, M. C.; Kang, P.; Nam, S. Mechanically Self-Assembled, Three-Dimensional Graphene-Gold Hybrid Nanostructures for Advanced Nanoplasmonic Sensors. *Nano Lett.* **2015**, *15*, 7684–7690.
- (31) Wang, M. C.; Chun, S.; Han, R. S.; Ashraf, A.; Kang, P.; Nam, S. Heterogeneous, Three-Dimensional Texturing of Graphene. *Nano Lett.* **2015**, *15*, 1829–1835.
- (32) Thomas, A. V.; Andow, B. C.; Suresh, S.; Eksik, O.; Yin, J.; Dyson, A. H.; Koratkar, N. Controlled Crumpling of Graphene Oxide Films for Tunable Optical Transmittance. *Adv. Mater.* **2015**, 27, 3256–3265.
- (33) Schriver, M.; Regan, W.; Gannett, W. J.; Zaniewski, A. M.; Crommie, M. F.; Zettl, A. Graphene as a Long-Term Metal Oxidation Barrier: Worse than Nothing. *ACS Nano* **2013**, *7*, 5763–5768.
- (34) Jiang, T.; Huang, R.; Zhu, Y. Interfacial Sliding and Buckling of Monolayer Graphene on a Stretchable Substrate. *Adv. Funct. Mater.* **2013**, 24, 396–402.
- (35) Brennan, C. J.; Nguyen, J.; Yu, E. T.; Lu, N. Interface Adhesion between 2D Materials and Elastomers Measured by Buckle Delaminations. *Adv. Mater. Interfaces* **2015**, *2*, 1500176.
- (36) Bronsgeest, M. S.; Bendiab, N.; Mathur, S.; Kimouche, A.; Johnson, H. T.; Coraux, J.; Pochet, P. Strain Relaxation in CVD Graphene: Wrinkling with Shear Lag. *Nano Lett.* **2015**, *15*, 5098–5104.
- (37) Kim, K.; Lee, Z.; Malone, B. D.; Chan, K. T.; Alemán, B.; Regan, W.; Gannett, W.; Crommie, M. F.; Cohen, M. L.; Zettl, A. Multiply Folded Graphene. *Phys. Rev. B: Condens. Matter Mater. Phys.* **2011**, *83*, 245433–245438.
- (38) Zhang, Y.; Wei, N.; Zhao, J.; Gong, Y.; Rabczuk, T. Quasi-Analytical Solution for the Stable System of the Multi-Layer Folded Graphene Wrinkles. *J. Appl. Phys.* **2013**, *114* (6), 063511.
- (39) Kunz, D. A.; Feicht, P.; Gödrich, S.; Thurn, H.; Papastavrou, G.; Fery, A.; Breu, J. Space-Resolved In-Plane Moduli of Graphene Oxide and Chemically Derived Graphene Applying a Simple Wrinkling Procedure. *Adv. Mater.* **2013**, *25*, 1337–1341.
- (40) Feicht, P.; Siegel, R.; Thurn, H.; Neubauer, J. W.; Seuss, M.; Szabó, T.; Talyzin, A. V.; Halbig, C. E.; Eigler, S.; Kunz, D. A.; Fery, A.; Papastavrou, G.; Senker, J.; Breu, J. Systematic Evaluation of Different Types of Graphene Oxide in Respect to Variations in Their In-Plane Modulus. *Carbon* **2017**, *114*, 700–705.
- (41) Liu, Z.; Amani, M.; Najmaei, S.; Xu, Q.; Zou, X.; Zhou, W.; Yu, T.; Qiu, C.; Birdwell, A. G.; Crowne, F. J.; Vajtai, R.; Yakobson, B. I.;

- Xia, Z.; Dubey, M.; Ajayan, P. M.; Lou, J. Strain and Structure Heterogeneity in MoS2 Atomic Layers Grown by Chemical Vapour Deposition. *Nat. Commun.* **2014**, *5*, 5246.
- (42) Zhang, K.; Arroyo, M. Adhesion and Friction Control Localized Folding in Supported Graphene. *J. Appl. Phys.* **2013**, *113*, 193501.
- (43) Zhang, K.; Arroyo, M. Understanding and Strain-Engineering Wrinkle Networks in Supported Graphene through Simulations. *J. Mech. Phys. Solid.* **2014**, *72*, *61*–74.
- (44) Gao, X.; Li, C.; Song, Y.; Chou, T.-W. A Continuum Mechanics Model of Multi-Buckling in Graphene—Substrate Systems with Randomly Distributed Debonding. *Int. J. Solid Struct.* **2016**, *97*–*98*, 510–519.
- (45) Ostadhossein, A.; Rahnamoun, A.; Wang, Y.; Zhao, P.; Zhang, S.; Crespi, V. H.; Van Duin, A. C. T. ReaxFF Reactive Force-Field Study of Molybdenum Disulfide (MoS2). *J. Phys. Chem. Lett.* **2017**, *8*, 631–640
- (46) Kim, H.-J.; Song, Y.-W.; Namgung, S. D.; Song, M.-K.; Yang, S.; Kwon, J.-Y. Optical Properties of the Crumpled Pattern of Selectively Layered MoS₂. Opt. Lett. **2018**, 43, 4590–4594.
- (47) Wu, Y.; Fuh, H.-R.; Zhang, D.; Coileáin, C. Ó.; Xu, H.; Cho, J.; Choi, M.; Chun, B. S.; Jiang, X.; Abid, M.; Liu, H.; Wang, J. J.; Shvets, I. V.; Chang, C-R.; Wu, H-C. Simultaneous Large Continuous Band Gap Tunability and Photoluminescence Enhancement in GaSe Nanosheets via Elastic Strain Engineering. *Nano Energy* **2017**, 32, 157–164.
- (48) Mei, H.; Landis, C. M.; Huang, R. Concomitant Wrinkling and Buckle-Delamination of Elastic Thin Films on Compliant Substrates. *Mech. Mater.* **2011**, *43*, 627–642.
- (49) Kunz, D. A.; Erath, J.; Kluge, D.; Thurn, H.; Putz, B.; Fery, A.; Breu, J. In-Plane Modulus of Singular 2:1 Clay Lamellae Applying a Simple Wrinkling Technique. *ACS Appl. Mater. Interfaces* **2013**, *5*, 5851–5855.
- (50) Castellanos-Gomez, A.; Roldán, R.; Cappelluti, E.; Buscema, M.; Guinea, F.; van der Zant, H. S. J.; Steele, G. A. Local Strain Engineering in Atomically Thin MoS₂. *Nano Lett.* **2013**, *13*, 5361–5366.
- (51) Quereda, J.; San-Jose, P.; Parente, V.; Vaquero-Garzon, L.; Molina-Mendoza, A. J.; Agraït, N.; Rubio-Bollinger, G.; Guinea, F.; Roldán, R.; Castellanos-Gomez, A. Strong Modulation of Optical Properties in Black Phosphorus through Strain-Engineered Rippling. *Nano Lett.* **2016**, *16*, 2931–2937.
- (52) Yang, S.; Wang, C.; Sahin, H.; Chen, H.; Li, Y.; Li, S.-S.; Suslu, L.; Peeters, F. M.; Liu, Q.; Li, J.; Tongay, S. Tuning the Optical, Magnetic, and Electrical Properties of ReSe2 by Nanoscale Strain Engineering. *Nano Lett.* **2015**, *15*, 1660–1666.
- (53) Deng, S.; Gao, E.; Xu, Z.; Berry, V. Adhesion Energy of MoS2 Thin Films on Silicon-Based Substrates Determined via the Attributes of a Single MoS2 Wrinkle. *ACS Appl. Mater. Interfaces* **2017**, 9, 7812–7818.
- (54) Ren, H.; Xiong, Z.; Wang, E.; Yuan, Z.; Sun, Y.; Zhu, K.; Wang, B.; Wang, X.; Ding, H.; Liu, P.; Zhang, L.; Wu, J.; Fan, S.; Li, X.; Liu, K. Watching Dynamic Self-Assembly of Web Buckles in Strained MoS₂ Thin Films. *ACS Nano* **2019**, *13*, 3106.
- (55) Han, E.; Yu, J.; Annevelink, E.; Son, J.; Kang, D. A.; Watanabe, K.; Taniguchi, T.; Ertekin, E.; Huang, P. Y.; van der Zande, A. M. Ultrasoft Slip-Mediated Bending in Few-Layer Graphene. *Nat. Mater.* **2019**, DOI: 10.1038/s41563-019-0529-7.
- (56) de Lima, A. L.; Müssnich, L. A. M.; Manhabosco, T. M.; Chacham, H.; Batista, R. J. C.; de Oliveira, A. B. Soliton Instability and Fold Formation in Laterally Compressed Graphene. *Nanotechnology* **2015**, *26*, 045707.
- (57) van der Zande, A. M.; Huang, P. Y.; Chenet, D. A.; Berkelbach, T. C.; You, Y.; Lee, G.-H.; Heinz, T. F.; Reichman, D. R.; Muller, D. A.; Hone, J. C. Grains and Grain Boundaries in Highly Crystalline Monolayer Molybdenum Disulphide. *Nat. Mater.* **2013**, *12*, 554–561.
- (58) van Der Zande, A. M.; Kunstmann, J.; Chernikov, A.; Chenet, D. A.; You, Y.; Zhang, X.; Huang, P. Y.; Berkelbach, T. C.; Wang, L.; Zhang, F.; Hybertsen, M. S.; Muller, D. A.; Reichman, D. R.; Heinz, T. F.; Hone, J. C. Tailoring the Electronic Structure in Bilayer

- Molybdenum Disulfide via Interlayer Twist. *Nano Lett.* **2014**, *14*, 3869–3875.
- (59) David, S. N.; Zhai, Y.; van der Zande, A. M.; O'Brien, K.; Huang, P. Y.; Chenet, D. A.; Hone, J. C.; Zhang, X.; Yin, X. Rapid, All-Optical Crystal Orientation Imaging of Two-Dimensional Transition Metal Dichalcogenide Monolayers. *Appl. Phys. Lett.* **2015**, *107*, 111902.
- (60) Gurarslan, A.; Yu, Y.; Su, L.; Yu, Y.; Suarez, F.; Yao, S.; Zhu, Y.; Ozturk, M.; Zhang, Y.; Cao, L. Surface-Energy-Assisted Perfect Transfer of Centimeter-Scale Monolayer and Few-Layer MoS2 Films onto Arbitrary Substrates. ACS Nano 2014, 8, 11522–11528.
- (61) Barzegar, H. R.; Gracia-Espino, E.; Yan, A.; Ojeda-Aristizabal, C.; Dunn, G.; Wågberg, T.; Zettl, A. C60/Collapsed Carbon Nanotube Hybrids: A Variant of Peapods. *Nano Lett.* **2015**, *15*, 829–834
- (62) Xu, P.; Kang, J.; Choi, J.-B.; Suhr, J.; Yu, J.; Li, F.; Byun, J.-H.; Kim, B.-S.; Chou, T.-W. Laminated Ultrathin Chemical Vapor Deposition Graphene Films Based Stretchable and Transparent High-Rate Supercapacitor. *ACS Nano* **2014**, *8*, 9437–9445.
- (63) Yu, H.-H.; Hutchinson, J. W. Influence of Substrate Compliance on Buckling Delamination of Thin Films. *Int. J. Fract.* **2002**, *113*, 39–55.
- (64) Deborde, T.; Joiner, J. C.; Leyden, M. R.; Minot, E. D. Identifying Individual Single-Walled and Double-Walled Carbon Nanotubes by Atomic Force Microscopy. *Nano Lett.* **2008**, *8*, 3568–3571.
- (65) Alizadegan, R.; Liao, A. D.; Xiong, F.; Pop, E.; Hsia, K. J. Effects of Tip-Nanotube Interactions on Atomic Force Microscopy Imaging of Carbon Nanotubes. *Nano Res.* **2012**, *5*, 235–247.
- (66) Yu, J.; van der Zande, A. M.; Ertekin, E. Evolution of Fold Morphology in Compressed Two-Dimensional Materials, to be submitted for publication, 2020.
- (67) Gant, P.; Huang, P.; de Lara, D. P.; Guo, D.; Frisenda, R.; Castellanos-Gomez, A. A Strain Tunable Single-Layer MoS2 Photo-detector. *Mater. Today* **2019**, *27*, 8–13.
- (68) Gong, L.; Kinloch, I. A.; Young, R. J.; Riaz, I.; Jalil, R.; Novoselov, K. S. Interfacial Stress Transfer in a Graphene Monolayer Nanocomposite. *Adv. Mater.* **2010**, 22, 2694–2697.
- (69) Scharfenberg, S.; Rocklin, D. Z.; Chialvo, C.; Weaver, R. L.; Goldbart, P. M.; Mason, N. Probing the Mechanical Properties of Graphene Using a Corrugated Elastic Substrate. *Appl. Phys. Lett.* **2011**, 98, 091908.
- (70) Zhang, Z.; Li, T. Determining Graphene Adhesion via Substrate-Regulated Morphology of Graphene. *J. Appl. Phys.* **2011**, 110 (5), 083526.
- (71) Zhu, L.; Chen, X. Delamination-Based Measurement and Prediction of the Adhesion Energy of Thin Film/Substrate Interfaces. *J. Eng. Mater. Technol.* **2017**, *139*, 021021.
- (72) Lee, C.; Wei, X.; Kysar, J. W.; Hone, J. Measurement of the Elastic Properties and Intrinsic Strength of Monolayer Graphene. *Science* **2008**, 321, 385–388.
- (73) Liu, K.; Yan, Q.; Chen, M.; Fan, W.; Sun, Y.; Suh, J.; Fu, D.; Lee, S.; Zhou, J.; Tongay, S.; Ji, J.; Neaton, J. B.; Wu, J. Elastic Properties of Chemical-Vapor-Deposited Monolayer MoS₂, WS₂, and Their Bilayer Heterostructures. *Nano Lett.* **2014**, *14*, 5097–5103.
- (74) De Heer, W. A.; Berger, C.; Ruan, M.; Sprinkle, M.; Li, X.; Hu, Y.; Zhang, B.; Hankinson, J.; Conrad, E. Large Area and Structured Epitaxial Graphene Produced by Confinement Controlled Sublimation of Silicon Carbide. *Proc. Natl. Acad. Sci. U.S.A.* **2011**, *108*, 16900–16905.